Supporting Information:

The Effect of Intrinsic Defects in Grain Boundaries on Non-Radiative Recombination in $CsPbI_3$ and $CsPbBr_3$

Lotte Kortstee[1], Noam Veber[2,3], Betty Shamaev[2,3], Yehonadav Bekenstein[2,3], Juan Maria García Lastra[1], Ivano E. Castelli[1]

[1] Department of Energy Conversion and Storage (DTU Energy), Technical University of Denmark, Agnes Nielsens Vej 301, DK-2800 Kongens Lyngby, Denmark
[2] Department of Materials Science and Engineering, Technion - Israel Institute of Technology, Haifa 3200003, Israel
[3] The Solid-State Institute, Technion - Israel Institute of Technology, Haifa 3200003, Israel

1 Bandstructures

We calculate the bandstructures of bulk $CsPbBr_3$ and $CsPbI_3$ (Figure 1) to assess if our combination of functionals is appropriate for describing bandstructure characteristics in these materials. We find bandgaps close to experimental results, showing a direct transition at the Γ-point, as we would expect. We therefore conclude that the HSE α parameter of 0.43 is ideal for describing the band edges and total energies of both material classes.

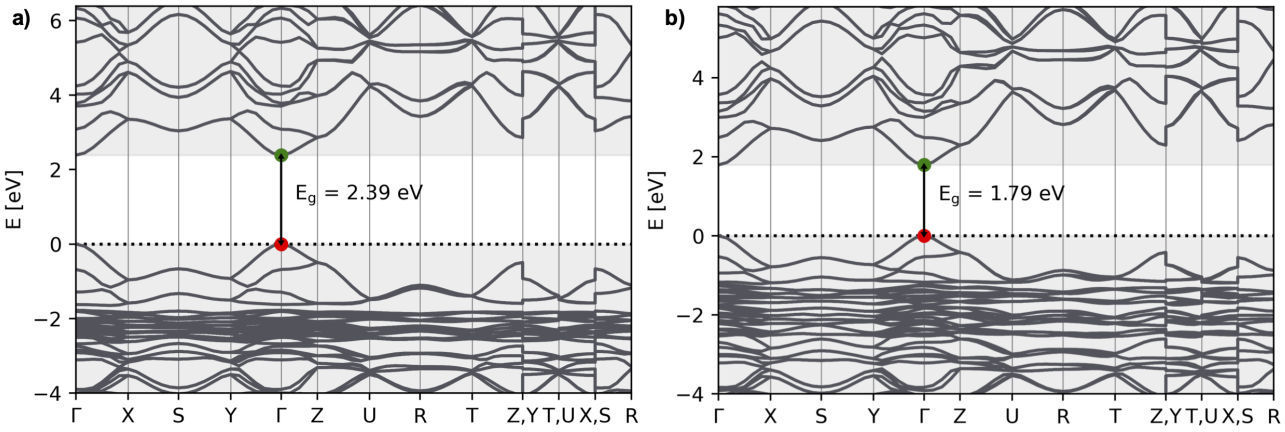

Figure 1: Electronic bandstructures of bulk $CsPbBr_3$ (**a**) and bulk $CsPbI_3$ (**b**). Both structures show a direct bandgap at the Γ-point.

2 Convergence of grain boundary structures and defect formation energies

Typically, a grain boundary separation of 20Å is recommended in halide perovskites to eliminate GB interactions introduced by the use of periodic boundary conditions.[1] However, due to the structural complexity of the grain boundary models and the limitations imposed by hybrid functionals on system size, our models achieve a separation of about 15 Å. To ensure that the bulk-like regions of these grain boundary structures remain well behaved, we evaluate the bandgap and the formation energy of the grain boundary plane and of a selection of

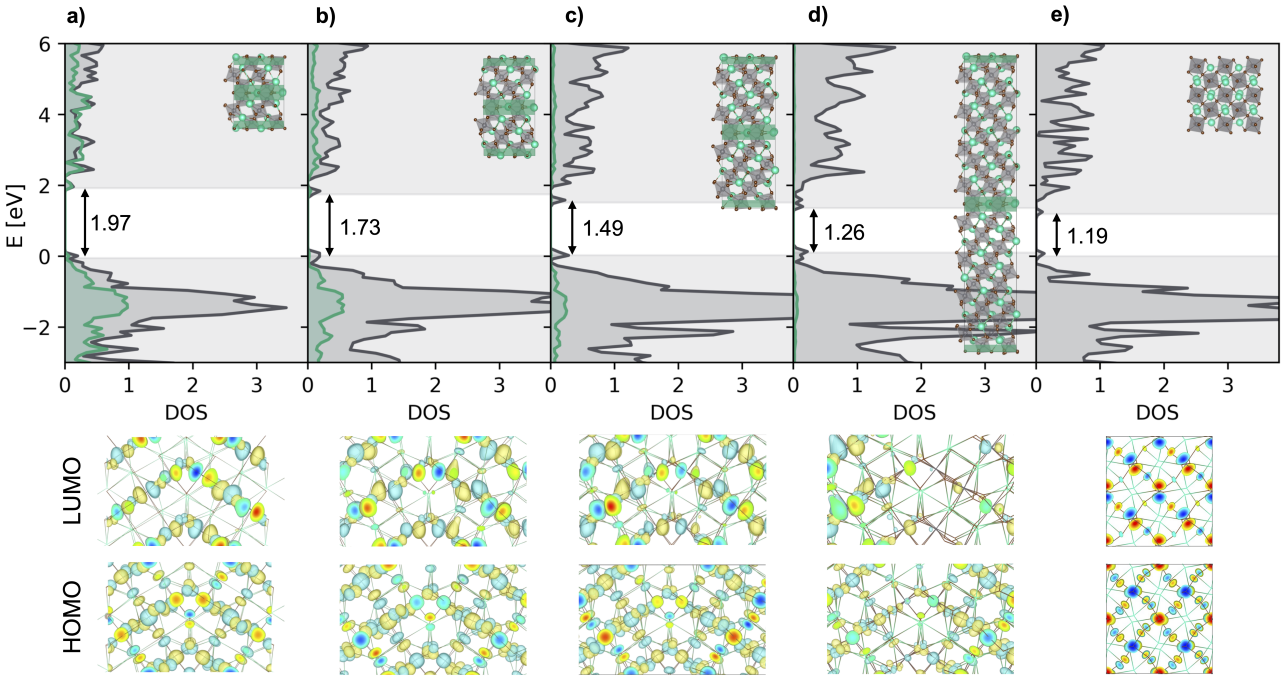

Figure 2: DOS of the Σ3(111) GB with varying inter GB-layer thickness from small to large (**a-d**). (**e**) shows the DOS of the bulk structure. The figure inset shows the structure of the various GB unit cells. DOS shows both contributions from the GB-layer, identified in green, and from the bulk-like region in between GB layers, identified as gray. For clarity, the atoms in the GB layers are colored in green in the figure insets. Below the DOS, we show the wavefunction of the HOMO and LUMO band for each grain boundary. Mind that the absolute gap is smaller than in Figure 1a because we compare structures at the PBE+SOC level instead of HSE.

defects as a function of unit cell size in the z-direction in $CsPbBr_3$ (i.e. separation between GB planes). We analyze these results at the PBE+SOC level, as the system sizes become too large for HSE single-point calculations. To understand how the band edges evolve with increasing GB separation, we evaluate the PDOS of the Σ3(111) GB in Figure 2, where the with GB-layer contributions highlighted in green and all other atoms in gray. As the separation in the z direction increases, the bandgap approaches the bulk value and converges at a GB spacing of ∼40Å (Figure 2d). To test whether the GB region exhibits distinct electronic behavior, we visualize the wavefunctions associated with the HOMO and LUMO for different GB sizes. In all cases, the GB contributes with the same types of orbitals to the band edges as the bulk region, indicating no separate electronic reservoir. Thus, electrons and holes near the band edges can be referenced to the bulk electronic structure. Because of the computational costs associated with performing defect calculations in systems of this size on the hybrid functional level, we evaluate instead whether the GB formation energy and defect formation energy depend on the interlayer distance.

We perform convergence tests in $CsPbBr_3$ GBs, on the defects most relevant to this study: the neutral defects Pb_i^0 and Br_i^0, as well as the charged defects Pb_i^{2+}, Br_i^{-1}, and Br_i^{+1}. This allows us to demonstrate convergence not only of the defect formation energies, but also of the charge transition levels. As done for our bandgap convergence test in grainboundaries presented in Figure 2, unit cells of varying size are used, expanded exclusively in the z-direction to increase the grain boundary interlayer distance with increasing atom count. We additionally verify that all defect relaxations converge to the same local minimum. For all charged defects, point-charge and potential-alignment corrections are included, and formation energies are calculated with the fermi level fixed at the VBM. Convergence analysis of Br_i^0 is terminated at a structure size of 240 atoms, as no further system-size dependence is observed and this charge state is not relevant for the charge transition levels.

As shown in Figure 3, defect formation energies, and consequently charge transition levels, are converged for 120-atom Σ3(112) structures and 160-atom Σ3(111) structures, for both neutral and charged defects. We therefore use these unit cell sizes to perform our defect analysis on. At the same time, Charge transition levels are aligned to the bulk band edges by referencing the VBM to the deep Cs_s state on a Cs-atom in the bulk-like region far from the defect, as our convergence tests show that these bandedges dominate in the GB area.

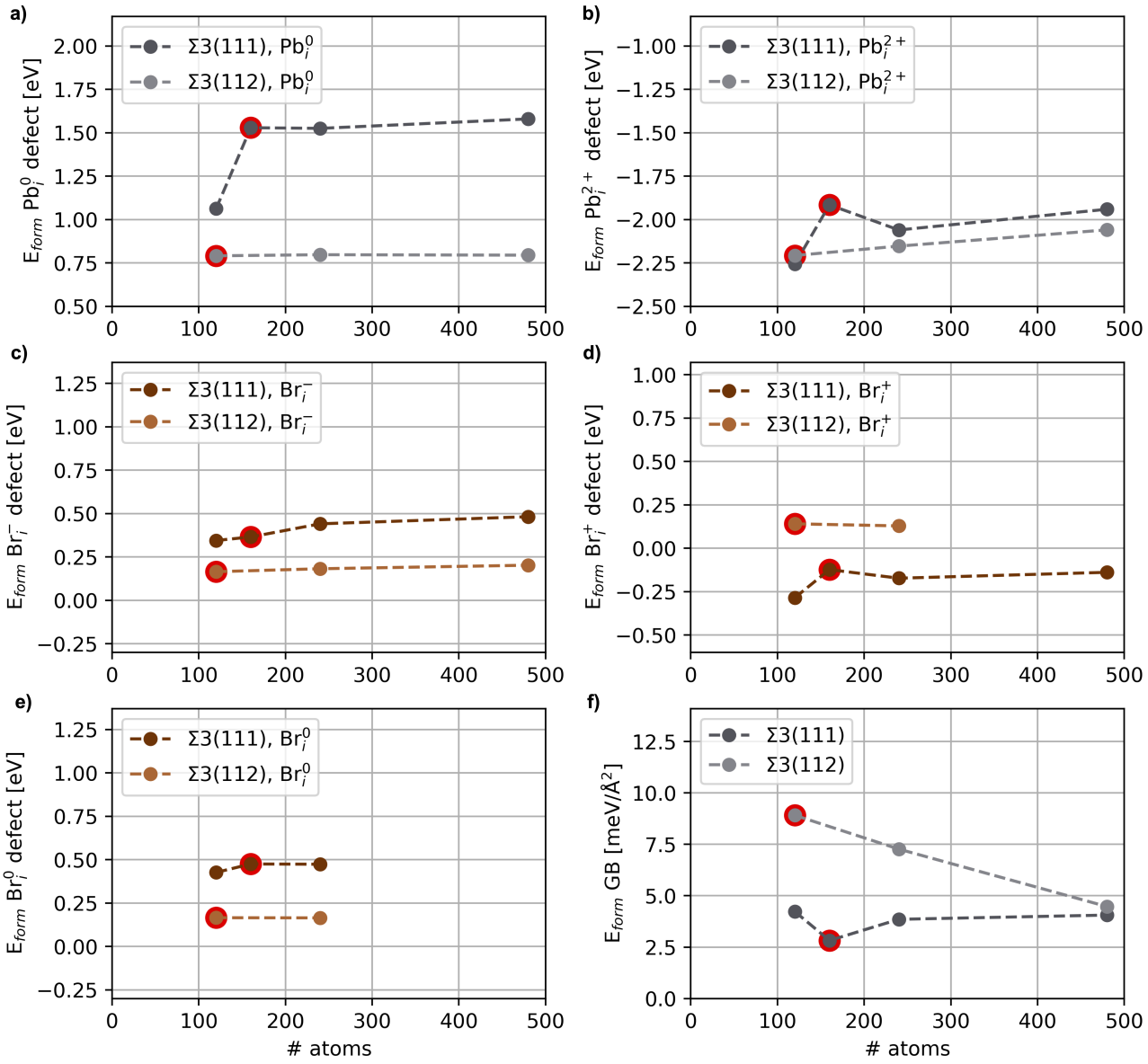

Figure 3: Defect formation energies of and the Pb_i^0, Pb_i^{2+}, Br_i^-, Br_i^+ and Br_i^0 defect sas a function of atoms in the grain boundary structure (**a**, **b**, **c**, **d** and **e** respectively). The red circled points signify the structures chosen to perform our defect analysis on presented in the paper. All defected structures relax to the same structural minimum. Formation energy of the grain boundary plane as a function of unit cell size (**f**).

Because HSE calculations severely limit the allowable cell size, we perform all computations on a broken-symmetry version of the grain boundary that reduces the periodicity along the x direction. We verify that this modification does not significantly affect the bulk-like region of the GB. For the Σ3(111) grain boundary, the fully periodic structure yields a bandgap of 1.51 eV, while the corresponding non-periodic structure in Figure 2c gives 1.49 eV. Moreover, starting from the GB geometry, we can reconstruct a bulk structure by removing the boundary. Singlepoint bandgap calculations on these reconstructed bulk cells recover the expected bulk bandgap (∼1.2 eV), confirming that the non-periodic GB model accurately represents the electronic behavior near the boundary. We also tested the impact on defect energetics. For the Pb_i^0 defect, the formation energy difference between the periodic and non-periodic GB structures is only 0.1 eV, acceptable within the frame of this level of theory.

3 Chemical Stability Window of $CsPbI_3$ and $CsPbBr_3$

We compute the chemical stability window by setting the constraints for $CsPbBr_3$ and $CsPbBr_3$ respectively:

$$\mu_{\mathrm{Cs}} + \mu_{\mathrm{Pb}} + 3 \cdot \mu_{\mathrm{Br}} = \Delta H_f(\mathrm{CsPbBr_3}) \tag{1a}$$

$$\mu_{\mathrm{Cs}} + \mu_{\mathrm{Pb}} + 3 \cdot \mu_{\mathrm{I}} = \Delta H_f(\mathrm{CsPbI_3}) \tag{1b}$$

Where the formation energy is calculated referenced against Cs metal, Pb metal, Br_2 molecule, and I solid. Outside of the chemical potentials forming the borders of these constraints, other possible phases become dominant. The chemical stability window is determined for bulk $CsPbBr_3$ and $CsPbI_3$, and is visualized in Figure 4. We use the same chemical stability constraints to indicate the Pb-rich/Pb-poor conditions the grain boundary structures.

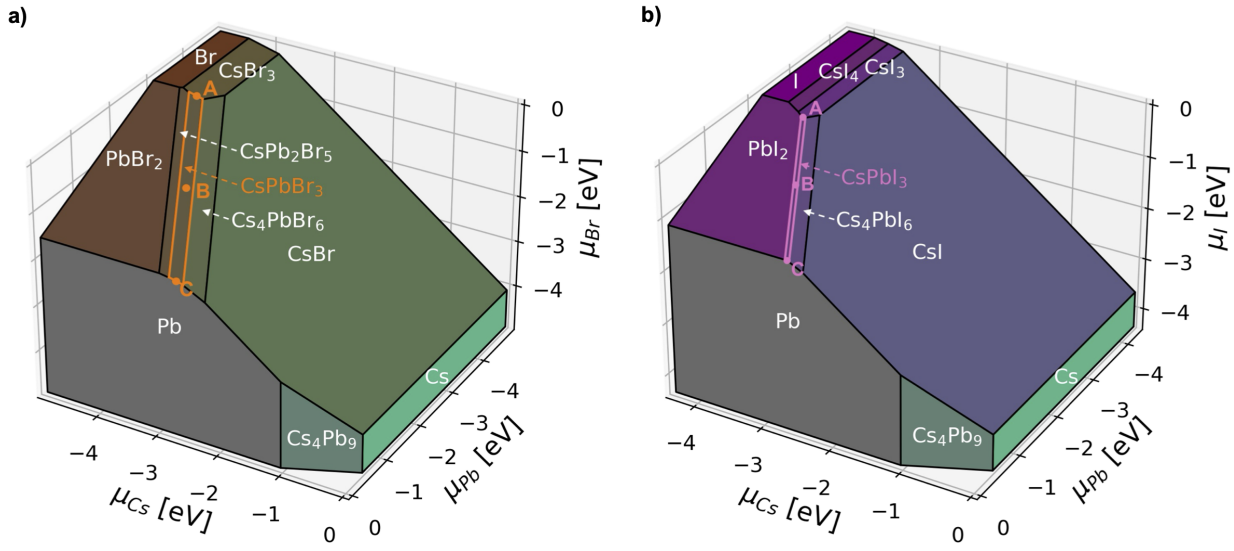

Figure 4: The chemical potential stability region of $CsPbBr_3$ (**a**) and $CsPbI_3$ (**b**). Within the stable region, point A,B and C are identified. Point A represents the Br-rich/Pb-poor synthesis conditions, and C represents Br-poor/Pb-rich synthesis conditions. Point B represents intermediate conditions.

4 Local structure of relaxed Pb_{halide} antisite defects

The structural characteristics of the Pb_{halide} defect reveal that the Pb atom takes the place in the lattice where it can attain the highest coordination number. This is in all studied cases enhanced by the grain boundary.

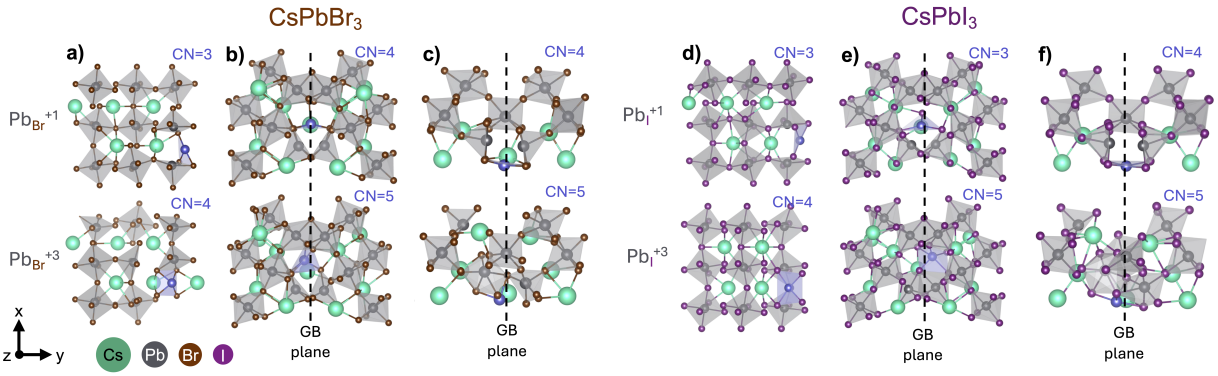

Figure 5: Defect geometries of Pb_{halide} antisites under varying charge in bulk, $\Sigma3(111)(0,0)$ and $\Sigma3(111)(0,0)$ are given in $CsPbBr_3$ (**a,b,c**) and $CsPbI_3$ (**d,e,f**) respectively. The lead antisite and its related octahedral are visualized in blue. A representative fraction of the grain boundaries is visualized and the grain boundary plane is indicated with a dotted line.

5 Defect formation under Pb-poor/Pb-rich conditions

An analysis of defect formation energy at Pb-poor (A) and Pb-rich (C) synthesis condition is appended in Figure 6. Strong p-type behavior is observed under Pb-poor conditions, whereas Pb-rich conditions push the character to be more n-type.

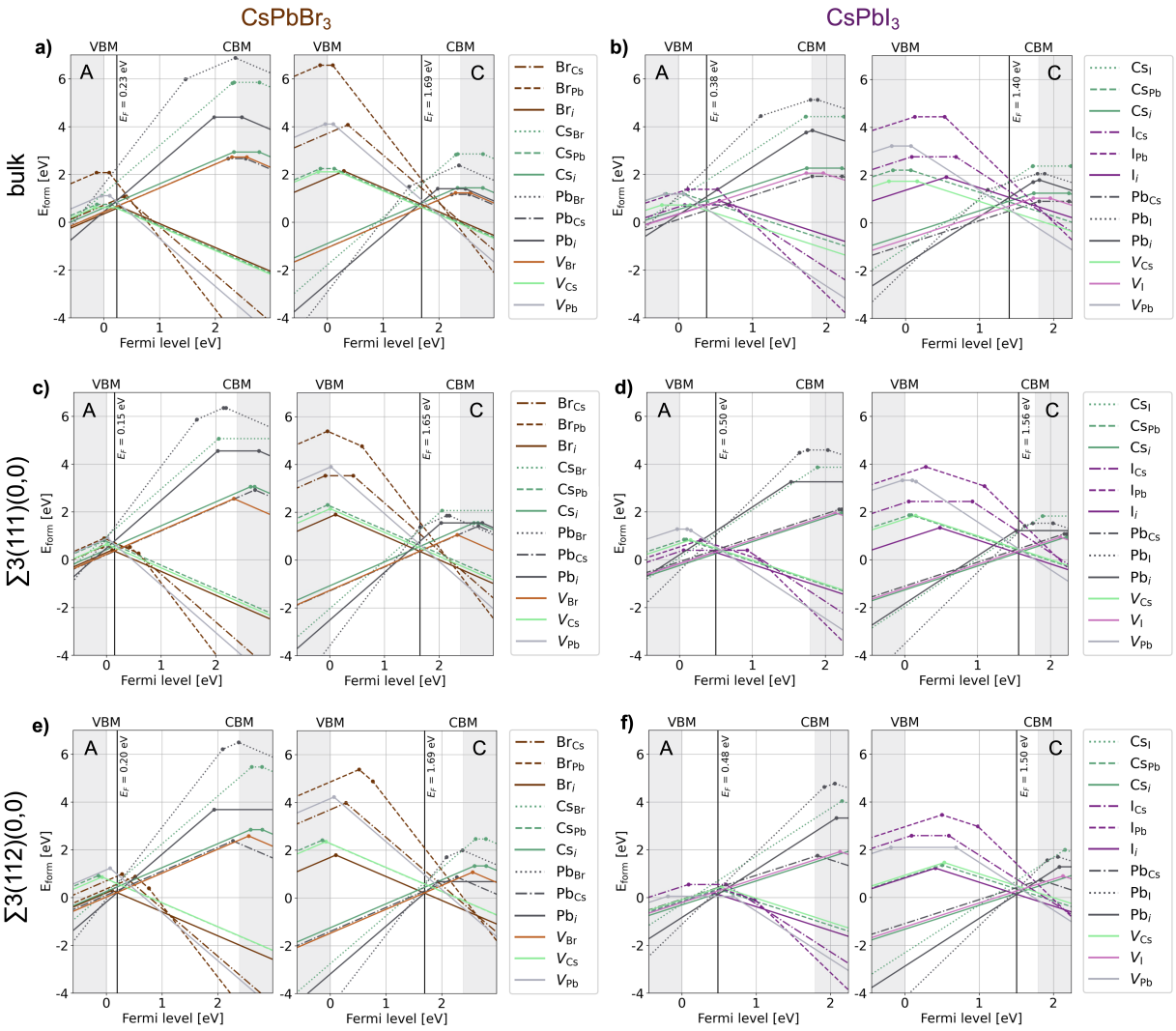

Figure 6: Formation energy of all possible intrinsic defects in $CsPbBr_3$ (**a,c,e**) and $CsPbI_3$ (**b,d,f**), in bulk geometry (**a,b**), and in grain boundaries Σ3(111) (**c,d**) and Σ3(112) (**e,f**). All figures on the left side show defect formation energies under halide-rich/Pb-poor conditions (point A). All figures on the right side show defect formation energies under halide-poor/Pb-rich conditions (point C). The vertical line indicates the natural fermi-level pinning.

6 Bader charge analysis

A bader charge analysis is carried out using the bader code from the Henkelman group.[2] To verify that the electronic structure resulting from the PBE+SOC relaxation and the HSE+SOC singlepoint calculation are both capable of describing the same oxidation state of present species, we assess the difference in charge around each atom from the PBE calculation and the HSE calculation. We find minimal differences in charge around each atom of maximum 0.18 Q for the Pb atom, and a consistent shift for each atom type. An example of the bader charge difference between the HSE+SOC single point calculation and the PBE+SOC for the Br_i defect in $CsPbBr_3$ bulk is visualized in Figure 7. We conclude that the PBE+SOC relaxed geometry is able of capturing the correct electronic landscape and it is therefore justified to use the PBE geometry as a starting point for the

HSE single point calculation.

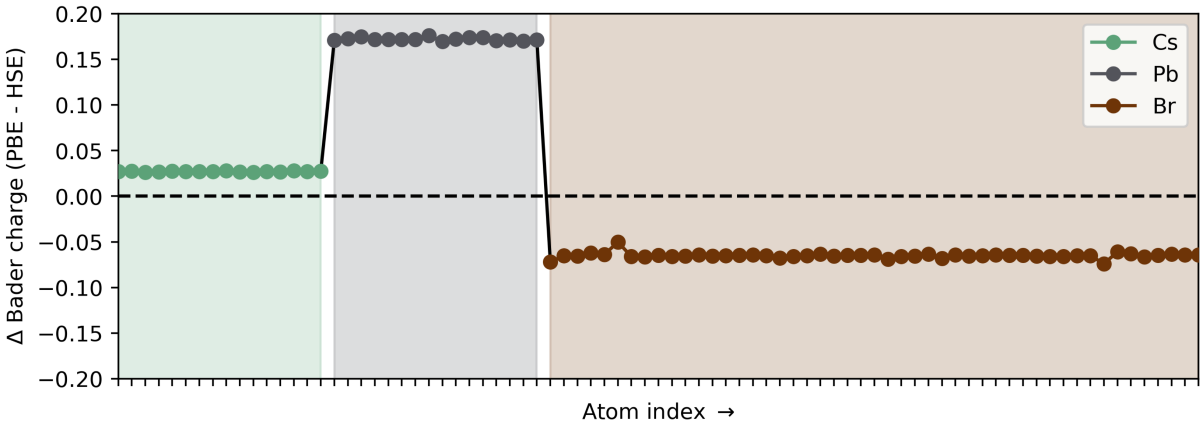

Figure 7: Difference in Bader charge between the PBE relaxation and the HSE singlepoint. Different atom species are signified with distinctive colours.

To ensure that the introduced charge is indeed localized on the interstitial atom, we further analyze the Bader charges of the halide and Pb interstitials in their various charge states. In Figure 8, we present the relative charge on each interstitial species. This relative charge is computed using Equation 2:

$$Q_{rel} = Q_{defect} - \bar{Q}_{lat} - Q_{formal} \tag{2}$$

Here Q_{rel} is the relative charge, Q_{defect} is the Bader charge associated to the interstitial atom, $\bar{Q}_{lat}$ is the average Bader charge over all other lattice atoms of the same species and Q_{formal} is the formal charge expected for that lattice species (e.g. -1 for a halide ion and +2 for Pb in the perovskite lattice).

These results show that the interstitials undergo changes in oxidation state depending on the charge introduced into the system. Because the relative charge is defined as the difference between the interstitial charge and the average charge of the corresponding lattice atoms, any substantial deviation reflects a change localized specifically on the interstitial atom.

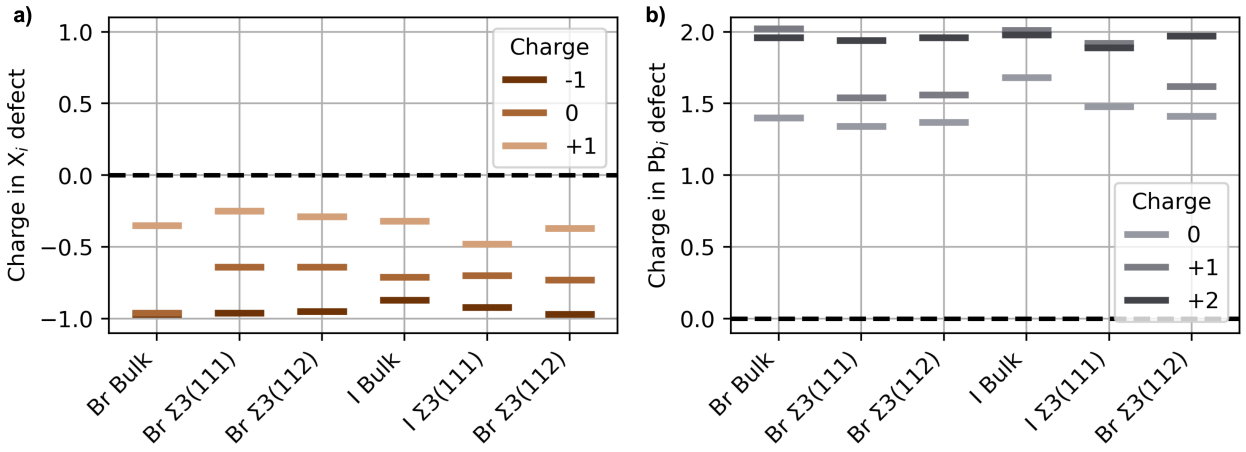

Figure 8: Charge on the interstitial atom depending on the amount of electrons added (negative charge) or removed (positive charge).

7 Cathodoluminescence Measurements of Grain Boundaries in Multidomain Crystals

Additional examples of cathodoluminescence (CL) maps are given in Figure 9a-b, showing both emission reduction along GBs and around inclusions. Compositional analysis using EDS of a particle shown in Figure 9c-d shows the expected perovskite stoichiometry in the crystal bulk, and excess of Pb at the location of an inclusion.

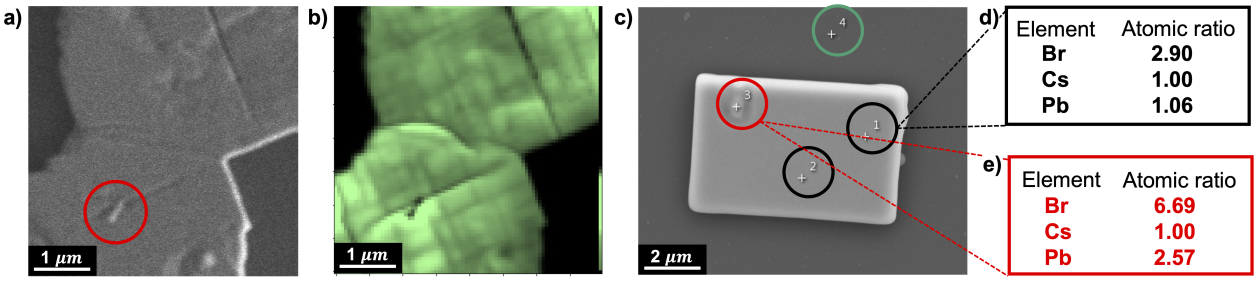

Figure 9: (**a**) SEM micrograph of multidomain $CsPbBr_3$ crystals, presenting different types of grain boundaries. A Pb rich inclusion on the boundary is highlighted by a red circle. (**b**) CL intensity map of the crystals presented in (**a**), showing reduced emission along the grain boundaries and dark regions at the locations of the inclusions. (**c**) SEM micrograph of a crystal with an inclusion from which four EDS measurements were taken. Measurements 1 and 2 were taken on the crystal's bulk (black circles) and presents atomic ratios consistent with CsPbBr3 as shown in (**d**). Measurement 3 (red circle) was taken from the inclusion and is found to be rich in Pb as shown in (**e**). Measurement 4 (green circle) was taken on the substrate for calibration and detected only Si and C.

8 eFVN corrections at the grain boundaries

eFNV point charge corrections[3] are applied to the charged supercells. We use the anisotropic dielectric tensor, which we calculate for bulk and for the Σ3(112) GB, to investigate if the GB has a large influence on the local screening. We compute for both dielectric tensors the eFNV correction term, and plot the difference as $\Delta E = E_{pc,\ bulk}\text{-}E_{pc,\ GB}$ in Figure 10. Note that at charge state 0 no charge corrections are necessary, therefore we have no data at this point. We can see that the difference in charge correction logically increases at higher charge, but the total difference is sufficiently small (<50 meV) to not have any major influence on the positioning of charge transition levels in the grain boundary. Based on these results, we use the bulk dielectric constant to correct point charges in the corresponding grain boundary systems.

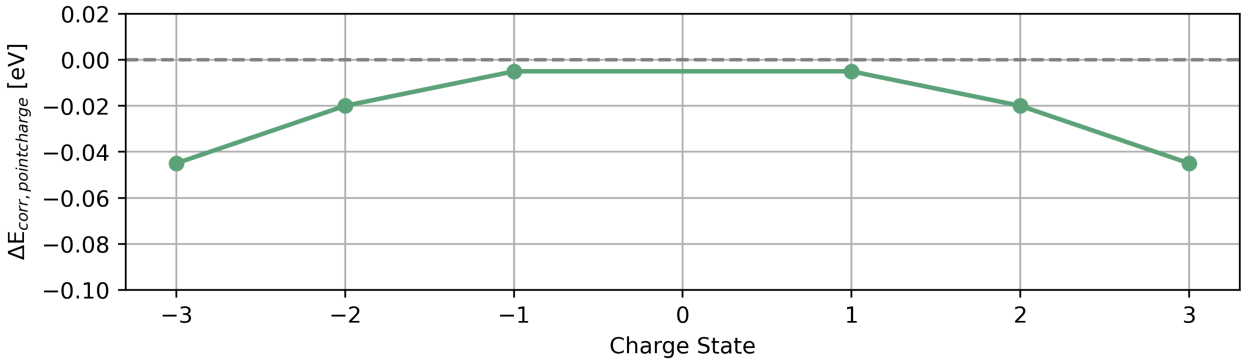

Figure 10: Difference in point charge correction to the total energy of the structure, calculated as $\Delta E = E_{pc,\ bulk}\text{-}E_{pc,\ GB}$, where $E_{pc,\ bulk}$ is the point charge correction using the bulk dielectric tensor and $E_{pc,\ GB}$ is the point charge correction using the GB dielectric tensor.

References

[1] Y. Guo, Q. Wang, and W. A. Saidi, "Structural stabilities and electronic properties of high-angle grain boundaries in perovskite cesium lead halides," *Journal of Physical Chemistry C*, vol. 121, pp. 1715–1722, 1 2017.

[2] W. Tang, E. Sanville, and G. Henkelman, "A grid-based bader analysis algorithm without lattice bias," *Journal of Physics Condensed Matter*, vol. 21, 2009.

[3] Y. Kumagai and F. Oba, "Electrostatics-based finite-size corrections for first-principles point defect calculations," *Physical Review B - Condensed Matter and Materials Physics*, vol. 89, 5 2014.